Dual energy subtraction method for breast calcification imaging

Vaia Koukou[a], Niki Martini[a], George Fountos[b,*], Christos Michail[b], Panagiota Sotiropoulou[a], Athanasios Bakas[c], Nektarios Kalyvas[b], Ioannis Kandarakis[b], Robert Speller[d], George Nikiforidis[a]

a Department of Medical Physics, Faculty of Medicine, University of Patras, 265 00, Patras, Greece

b Radiation Physics, Materials Technology and Biomedical Imaging Laboratory, Department of Biomedical Engineering, Technological Educational Institute of Athens, Egaleo, 122 10 Athens, Greece

c Medical Radiological Technology, Faculty of Health and Caring Professions, Technological Educational Institution of Athens, 122 10 Athens, Greece

d Department of Medical Physics and Bioengineering, University College London, Malet Place, Gower Street, London WC1E 6BT, UK

* Address correspondence to: George Fountos, gfoun@teiath.gr

Abstract

The aim of this work was to present an experimental dual energy (DE) method for the visualization of microcalcifications (μCs). A modified radiographic X-ray tube combined with a high resolution complementary metal-oxide-semiconductor (CMOS) active pixel sensor (APS) X-ray detector was used. A 40/70 kV spectral combination was filtered with 100 μm cadmium (Cd) and 1000 μm copper (Cu) for the low/high-energy combination. Homogenous and inhomogeneous breast phantoms and two calcification phantoms were constructed with various calcification thicknesses, ranging from 16 to 152 μm. Contrast-to-noise ratio (CNR) was calculated from the DE subtracted images for various entrance surface doses. A calcification thickness of 152 μm was visible, with mean glandular doses (MGD) in the acceptable levels (below 3 mGy). Additional post-processing on the DE images of the inhomogeneous breast phantom resulted in a minimum visible calcification thickness of 93 μm (MGD=1.62 mGy). The proposed DE method could potentially improve calcification visibility in DE breast calcification imaging.

Key words: breast imaging, dual energy, calcifications, X-rays, post-processing

1. Introduction

Breast cancer is a significant public health problem in the world up to date and is one of the most common, accounting for approximately 12% of globally diagnosed cancers in 2012 [1]. Among women, 16% of cancer deaths are attributed to breast cancer [2]. Early detection through screening and adequate follow-up of women with positive findings could significantly reduce breast cancer mortality (by 15-25%) [2].

Mammography is the standard method for early detection of breast carcinomas [3]. Microcalcifications (μCs) act as an early indicator of the presence of breast cancer [4] and are found in around 86% of mammograms in women aged 76-79 years [5]. A percentage of 30 to 50% of non-palpable breast cancers are detected solely through the appearance of μCs during a mammogram scan [6]. Furthermore, 93% of the ductal carcinoma in situ (DCIS), that is the most common type of non-invasive breast cancer, is detected due to presence of calcifications in the mammograms [7]. Calcifications are characterized as μCs when their size is in the range of 0.1-1.0 mm. The great majority of clustered calcifications have been proven to be within benign lesions (approximately 80% of biopsies) and about 20% of these are cancerous usually with no signs of tissue invasion [8]. However, since they are the smallest objects that can be detected, any further improvement in the detection and visualization of calcifications is an important step forward. Microcalcifications exhibit higher X-ray attenuation than the surrounding breast tissue making them visible, while masses are difficult to be detected because the X-ray attenuation is similar to that of the healthy breast tissue [9]. However, visualization of μCs could be obscured in mammograms by overlapping tissue structures. Therefore, small μCs could be extremely difficult to be detected even if the signal-to-noise ratio (SNR) is high [10] and [11]. Thus, their detection suffers from a high false negative rate [12].

Dual energy digital mammography (DEDM) can suppress the contrast between adipose and glandular tissues improving the detectability of μCs and masses [13],[14] and [15]. This technique requires two digital images, obtained with low- and high-energy X-ray spectra. Weighted subtraction of the logarithmic transform of these images is then performed to obtain a subtracted image that enhances μCs [10],[16].

Although dual energy (DE) imaging could suppress the tissue-structure background, it also increases the intrinsic noise in the DE images [10],[17],[18] and [19].

Over the last decades, several researchers studied the capability of DE mammography to detect microcalcifications and/or masses. Johns and Yaffe worked on a theoretical optimization considering an ideal imaging system [13]. Considering monoenergetic X-rays, the optimum pair of energies was 19 and 68 keV, for the low- and high-energy images, respectively. The experimental evaluation was accomplished with a prototype digital scanned projection radiography system using X-ray beams at 50 and 115 kV [20]. Brettle and Cowen [11] extended the theoretical model of Boone and Shaber [21] who studied novel detector combinations for energies close to those proposed in a previous study [13]. Asaga et al applied DEDM method to clinical examinations using a molybdenum anode tube at 28 and 40 kV and a computed radiography system [22]. The GE Senographe 2000D unit featuring dual-track anodes (Mo and Rh) was used in DE studies for μC detection, with tube voltages ranging from 25 to 49 kV and a hydrogenated amorphous silicon (aSi:H) flat panel detector coupled with a thallium-doped cesium iodide (CsI:Tl) converter layer [17],[18] and [19]. The same configuration was used in another study aiming to the detection of masses [15]. Furthermore, the use of dual energy iodine-based contrast enhanced digital mammography (CEDM) has been evaluated for the improvement in the detection of lesions [23] and [24]. Digital X-ray detectors, based on complementary metal oxide semiconductor (CMOS) active pixel sensors (APS), have been recently introduced in medical imaging applications [25], [26] and [27]. A pixel pitch smaller than 70-100 μm, that is currently available in flat panels, can improve the detection and characterization of μCs [28].

In a previous simulation study [29], we investigated a dual energy method incorporating a modified radiographic X-ray unit combined with a high resolution CMOS sensor. Initially, monoenergetic X-ray beams were studied in the range between 15 and 90 keV, at 1 keV increments. The optimum monoenergetic pair was 23 keV and 58 keV for the low- and high-energy, respectively. An approximation to monoenergetic beams was followed using polyenergetic X-ray spectra under K-edge filtration [29], [30], [31] and [32]. Various peak voltages, filter materials and thicknesses were examined in order to obtain spectra with mean energies similar to the optimal monoenergetic pair. This was achieved by 40/70 kV spectra combination

filtered with 100 μm cadmium (Cd) and 1000 μm copper (Cu) for the low/high energy, respectively.

In the current study, an experimental DE method is presented based on the simulation exposure conditions. The integrated prototype system used, consisted of a modified tungsten (W) anode X-ray tube combined with a high resolution CMOS APS sensor (pixel pitch of 22.5 μm), coupled with a 33.91 mg/cm^2 terbium-doped gadolinium oxysulfide (Gd_2O_2S:Tb) scintillator screen. Custom-made homogenous and inhomogeneous breast phantoms and two different calcification phantoms, as well as, the ACR mammography accreditation phantom were used. Furthermore, post-process noise reduction was applied on the dual energy images.

2. Materials and Methods

2.1. Experimental image acquisition process

The Del Medical Eureka radiographic system [33] with the following characteristics was used: W anode, 3 mm aluminum (Al) nominal inherent filtration, maximum load 50 kW, tube voltage range 40-150 kV and focal spot size 0.6 mm. The added filtration was 100 μm Cd (Alfa Aesar 11371, 99.9975%) at 40 kV and 1000 μm Cu (PTW 99.99%) at 70 kV for the low- and high-energy spectra, respectively. The detection system that was used, consisted of a Gd_2O_2S:Tb phosphor screen (Min-R 2190 with mass thickness of 33.91 mg/cm^2) coupled to an optical readout device including a CMOS Remote RadEye HR photodiode pixel array. The CMOS photodiode array has a format of 1200×1600 pixels, corresponding to an active area of 27 mm×36 mm, with a pixel pitch of 22.5 μm. The Gd_2O_2S:Tb screen was directly overlaid onto the active area of the CMOS (no fiber optic plate or coupling gel were used) [34] and [35]. This scintillator was selected due to its higher detective quantum efficiency (DQE) compared to other scintillators [34], [35] and [36]. The source-to-detector distance (SDD) was set at 66 cm and no antiscatter grid was used during image acquisitions. A Radcal 2026C dosimeter was positioned at the surface of the breast phantom and the entrance surface dose (ESD) was measured for various tube current-time products (400, 200 mA s for the LE and 250, 200 mAs for the HE). Mean glandular dose (MGD) was calculated using Eq. (1) [37]:

$$MGD = DgN\ ESD \quad (1)$$

Normalized glandular dose (*DgN*) data for a 4 cm breast thickness of 0% and 100% glandularity were obtained from published data [38]. Then, *DgN* values of 0% and 100% glandularity were fitted with a modified Fermi-Dirac distribution function [29]. For 50% glandular tissue the averaged MGD value was used. MGD was calculated for the low- and the high-energy exposures and then summed to obtain the total MGD. The ESD and MGD values for the LE and HE image acquisitions are shown in Table 1.

Table 1

ESD and MGD values for 50% glandularity.

ESD (mGy)			**MGD (mGy)**		
LE	**HE**	**Total**	**LE**	**HE**	**Total**
2.28	0.97	3.25	1.27	1.12	2.39
2.28	0.78	3.06	1.27	1.00	2.27
1.14	0.97	2.11	0.62	1.12	1.74
1.14	0.78	1.92	0.62	1.00	1.62

Weighted log-subtraction was used to generate the DE subtraction images, according to Eq. (2):

$$\ell n(DE) = \ell n(HE) - w\ell n(LE) \quad (2)$$

where HE and LE are the high- and low-energy images, and w is the weighting factor.

For each pair of low- and high-energy images, a number of DE images were generated for various weighting factors in the range of 0 to 1, at 0.1 intervals. The standard deviation (σ) of various background regions in the inhomogeneous breast phantom was calculated using a custom-developed algorithm. For the minimum σ, the corresponding w was selected. A w factor of 0.6 was adopted in the whole study, as indicated by the inhomogeneity.

The CNR was defined as the ratio of the absolute mean signal difference between calcification and background regions divided by the standard deviation of the background:

$$CNR_{DE} = \frac{\left|\overline{S_C} - \overline{S_B}\right|}{\sigma_B} \quad (3)$$

where C and B denote the calcification and background regions [39].

The target signal ($\overline{S_c}$) was obtained as the mean pixel value over a 21×21 pixels region of interest (ROI) in the middle of the circular region, while the mean surrounding background ($\overline{S_B}$) was estimated by averaging six regions of the same size located at positions around the target (for better statistics). The corresponding standard deviation (σ_B) was also obtained from the mean surrounding background regions. The CNR_{DE} threshold value for calcification visibility was 3 [10].

2.2. Phantoms

2.2.1. Custom-made breast phantoms

2.2.1.1. Homogenous phantom

Initially, a homogeneous breast phantom was used in order to validate the simulation study. Polyethylene (PE) and polymethyl methacrylate (PMMA) slabs were used as adipose and glandular tissue equivalent materials, respectively [40]. These materials were selected due to their similarity to breast tissue X-ray transmission properties. The total breast thickness was 4 cm, consisting of 50/50 (w/w) PE/PMMA slabs. Each slab had uniform thickness, with dimensions of 10 cm×10 cm.

2.2.1.2. Inhomogeneous phantom

An inhomogeneous phantom, composed of lard and fresh egg whites, was used to simulate adipose and glandular tissue, respectively, since they have similar composition to the corresponding human tissues [41] and [42]. Lard and fresh egg whites were placed in a tank, constructed by 0.5 cm thick PMMA slabs with dimensions of 10 cm×10 cm×4 cm, in a proportion of 50% w/w. The mixture was produced in our laboratory according to the method described by Freed et al [41] and [42].

2.2.1.3.Custom-made calcification phantoms

Two different calcification phantoms were constructed. The two PMMA slabs used, had dimensions of 10 cm×10 cm and thicknesses of 0.2 and 0.4 cm. In each slab, five holes of 3 mm diameter were drilled and filled with a mixture of epoxy resin and hydroxyapatite (HAp), described chemically as $Ca_5HO_{13}P_3$ (FLUKA 21223, ≥ 90% purity). The various HAp thicknesses were obtained using different proportions of epoxy resin and HAp. The proportions were calculated according to Eq. (4):

$$\frac{m_{HAp}}{m_{epoxy}} = \frac{t_{HAp} d_{HAp}}{\left(T \quad t_{HAp}\right) d_{epoxy}} \tag{4}$$

where m_{HAp}, m_{epoxy} are the masses of the HAp and epoxy resin (g), T is the thickness of the PMMA slab (cm), t_{HAp} and d_{HAp} are the thickness (cm) and density (3.18 g/cm^3) [43] of HAp, respectively and d_{epoxy} is the density of epoxy resin (1 g/cm^3).

The calcification phantoms are referred to as *C1* and *C2* phantoms corresponding to the 0.2 and 0.4 cm PMMA thicknesses, respectively. The HAp thicknesses, as well as, the corresponding masses of HAp and epoxy resin in the *C1* and *C2* phantoms, are shown in Table 2. The calcification thicknesses will be referred as 16, 31, 46, 61, 76 μm for *C1*, and 31, 61, 93, 122, 152 μm for *C2*. The calcification phantoms were placed below the breast phantoms.

Table 2

Calcification thicknesses and corresponding masses used in *C1* and *C2* phantoms.

Masses (g)		**Calcification thicknesses (μm)**	
HAp	**Epoxy resin**	***C1* phantom**	***C2* phantom**
0.02	0.62	15.85	31.70
0.03	0.68	30.77	61.54
0.06	0.78	46.32	92.63
0.10	1.01	60.76	121.52

0.14	1.12	75.70	151.40

213

214 *2.2.2. Accreditation phantom*

215 The mammographic accreditation phantom RMI model 156 (Fig. 1) was also used for
216 a perception of the calcification size and further verification of the present method
217 [44]. Since the aim of this study is the calcification visibility, the calcification specks
218 groups were selected for irradiation. The phantom specks with diameters 540 μm (7),
219 400 μm (8), 320 μm (9), 240 μm (10), and 160 μm (11) correspond to an equivalent
220 hydroxyapatite attenuation of 234.68, 173.71, 138.90, 104.14 and 69.40 μm ,
221 respectively.

222

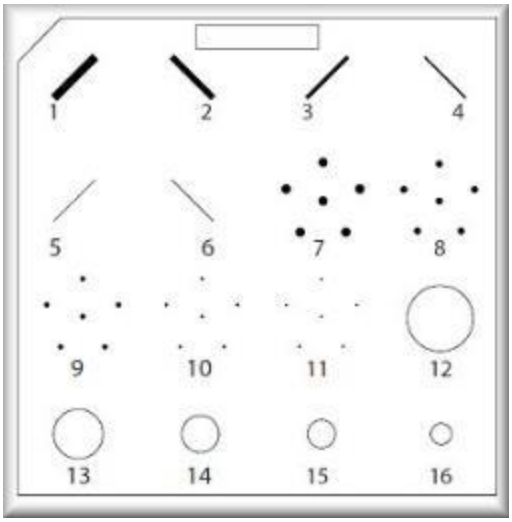

223

224 **Fig. 1.** ACR accreditation phantom.

225

226 Table 3 summarizes the details of the used phantoms.

227

228 **Table 3**

229 Summary of phantoms used.

Phantom number	Type	Features	Comments
1	*Homogenous breast phantom*	PE / PMMA slabs (50/50 w/w)	T = 4 cm
2	*Inhomogeneous breast phantom*	Lard / Egg whites (50/50 w/w)	T = 4 cm
3	Calcification phantom – C_1	Thicknesses:	Mixture of epoxy resin

4	Calcification phantom – C_2	16, 31, 46, 61, 76 μm Thicknesses: 31, 61, 93, 122, 152 μm	and hydroxyapatite - holes of 3 mm diameter
5	ACR accreditation phantom	Speck groups of various sizes	Equivalent HAp thicknesses were computed

230

231 *2.3. Post-processing of the DE images*

232 As aforementioned, the used CMOS APS X-ray detector has a pixel size of 22.5 μm,
233 which is much smaller compared to those used in previous dual energy studies
234 [15],[17],[18] and [19]. This pixel pitch corresponds to the highest resolution that can
235 be achieved, with lower SNR values. Such a small pixel pitch allows pixel binning in
236 order to increase the SNR. Pixel binning is a simple method in which the signal in
237 squares of neighboring pixels is averaged off-chip (after the signal is read-out).
238 Hereto, the binning method was applied on the DE images generated by the lowest
239 examined dose (MGD=1.62 mGy). Kernel sizes of 2×2, 3×3 and 4×4 were tested,
240 resulting in effective pixel sizes of 45, ~68 and 90 μm, respectively. For the DE
241 images of the inhomogeneous breast phantom, we studied how pixel binning affects
242 the measured CNR_{DE} values. Post-processing of the DE images of the ACR phantom
243 was also included.

244

245 **3. Results**

246 Figure 2 shows the experimental Cd and Cu filtered spectra at 40 and 70 kV
247 respectively, measured with a portable Amptek XR-100T spectrometer, based on a
248 Cadmium Telluride (CdTe) crystal-solid-state detector [31]. The corresponding mean
249 energies for the low- and high-energy spectra were 26 keV and 55 keV, resulting in
250 29 keV difference between the two spectra.

251

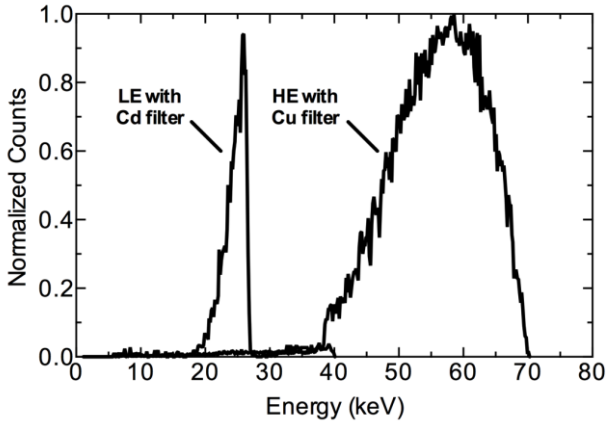

Fig. 2. LE spectrum at 40 kV filtered with 100 μm Cd and HE spectrum at 70 kV filtered with 1000 μm Cu.

3.1. Custom-made breast phantoms

Two different *C* phantoms were constructed and irradiated with various beam conditions. Dual energy images were obtained after applying the logarithmic weighted subtraction technique.

Table 4 shows the measured CNR_{DE} values of the C_1 and C_2 phantoms and all examined ESD/MGD values, for the homogenous and inhomogeneous breast phantoms. For calcification thicknesses existing in more than one *C* phantom the CNR_{DE} values correspond to the averaged CNR_{DE} values (i.e. 31 μm and 61 μm thick calcifications). The calcification thicknesses of 16μm and 31μm of C_1 and C_2 phantoms, respectively, could not be depicted either in the LE or DE image.

Calcification thickness of 152 μm was visible in both homogenous and inhomogeneous phantoms, as yielded CNR_{DE} values above the threshold of 3. For the former, this applies to MGD ranging from 1.74 to 2.39 mGy, while in the latter, only to the higher MGD value (2.39 mGy).

Table 4

CNR_{DE} values of C_1 and C_2 phantoms for the homogenous and the inhomogeneous breast phantom.

Breast Phantom	ESD/MGD (mGy)	CNR_{DE} 31 μm	CNR_{DE} 46 μm	CNR_{DE} 61 μm	CNR_{DE} 76 μm	CNR_{DE} 93 μm	CNR_{DE} 122 μm	CNR_{DE} 152 μm
Homogenous	3.25/2.39	0.71	1.03	1.85	2.10	2.32	2.85	3.47

	3.06/2.27	0.56	0.85	1.78	1.92	2.14	2.23	3.02
	2.11/1.74	0.62	0.92	1.81	1.98	2.25	2.61	3.05
	1.92/1.62	0.49	0.71	1.69	1.82	2.01	2.14	2.78
Inhomogeneous	3.25/2.39	0.45	0.84	1.40	1.56	1.76	2.28	3.05
	3.06/2.27	0.34	0.66	1.11	1.22	1.40	1.88	2.09
	2.11/1.74	0.38	0.72	1.17	1.29	1.60	2.07	2.37
	1.92/1.62	0.21	0.60	1.07	1.14	1.31	1.76	1.86

Figure 3 shows indicative DE images of the 4 cm thick homogenous phantom combined with C_1, C_2 phantoms for MGD of 1.62 mGy.

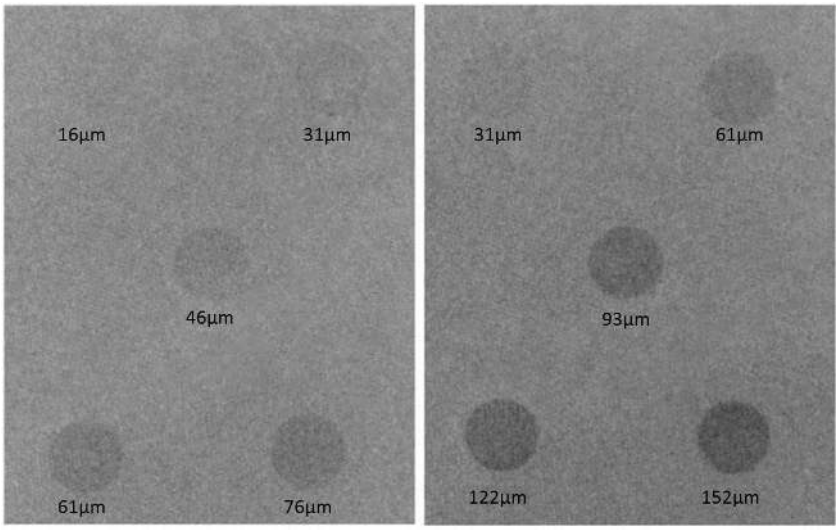

Fig. 3. DE images of the homogenous phantom with C_1 (left) and C_2 (right) phantoms.

Figure 4 shows indicative LE and DE images of the 4 cm thick inhomogeneous phantom combined with C_1, C_2 phantoms for the lowest MGD. The calcification thicknesses ranged from 16 μm to 76 μm and 31 μm to 152 μm in the C_1 and C_2 phantoms, respectively. The calcification thicknesses of 31 μm and 46 μm in C_1 phantom and 61 μm in C_2 phantom that are obscured in LE images are revealed in DE images, due to the suppression of the background structures. Furthermore, for the calcifications depicted in both LE and DE images (i.e. 61 μm in C_1 phantom, 122 μm in C_2 phantom) their margins appear to be more distinct in DE images.

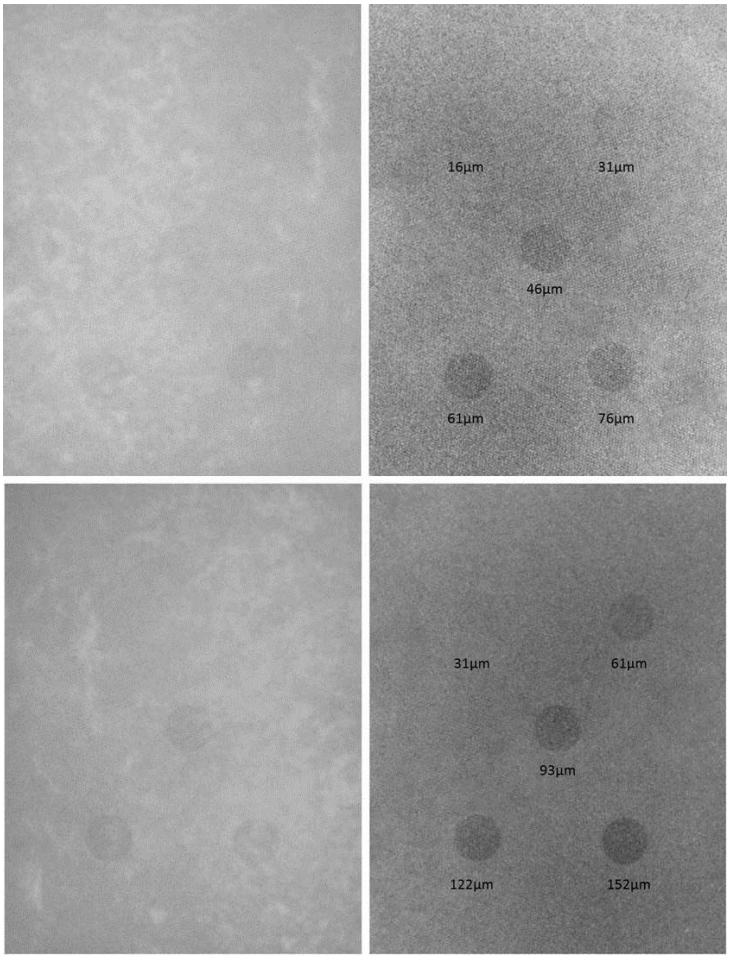

Fig. 4. LE (left) and DE (right) images of the inhomogeneous phantom for MGD of 1.62 mGy. C_1 phantom images (top row) and C_2 phantom images (bottom row).

The CNR_{DE} values of the post-processed DE images of C_1 and C_2 phantoms combined with the inhomogeneous breast phantom are presented in Table 5. Similarly, for calcification thicknesses existing in both calcification phantoms, the averaged CNR_{DE} is used. In the original DE image (bin 1×1) the CNR_{DE} values of all calcifications were below the threshold. The visible calcification thickness was reduced to 93 µm with improved CNR_{DE} values (greater than 3) for kernel sizes of 3 and 4 pixels. However, calcification thicknesses ranging from 31 to 76 µm were not visible in any of the processed DE calcification images.

Table 5

CNR_{DE} values of C_1 and C_2 phantoms for the post-processed inhomogeneous breast phantom DE images.

Calcification thickness (μm)	CNR_{DE}			
	Bin 1×1	**Bin 2×2**	**Bin 3×3**	**Bin 4×4**
31	0.21	0.44	0.70	0.83
46	0.60	0.80	0.98	1.38
61	1.07	1.74	2.03	2.46
76	1.14	2.05	2.51	2.95
93	1.31	2.62	3.16	3.50
122	1.76	2.95	3.52	3.90
152	1.86	3.16	3.89	4.11

Figure 5 shows a section of the original DE image (lowest MGD, 1.62 mGy) of the inhomogeneous breast phantom combined with the C_2 phantom and the same section of the binning image with a 4×4 kernel size. The margins of the left calcification (31 μm) appear more clearly in the post-processed image due to noise reduction.

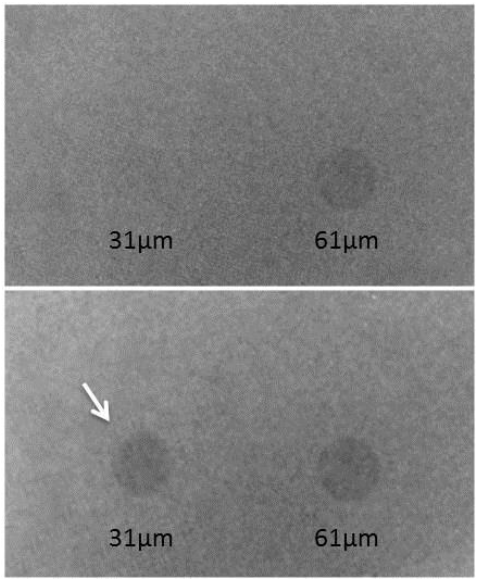

Fig. 5. Same section of the inhomogeneous phantom image combined with the C_2 phantom, without (top) and with (bottom) pixel binning using a 4×4 kernel. The calcification thickness of 31 μm (arrow) is enhanced in the binning image.

316

317 *3.2. Accreditation phantom*

318 Figure 6 shows two sections of the accreditation phantom containing the speck groups
319 (7) and (8) (diameters 540 μm and 400 μm, corresponding to 234.68 μm and 173.71
320 μm hydroxyapatite, respectively) for all MGD values. The μCs of the specks group
321 (7) were visible in all DE images, Figs. 6(a-d). All the details of the specks group (8)
322 were visible in Figs. 6(e-f), while the specks were barely visible in Figs. 6(g-h).

323

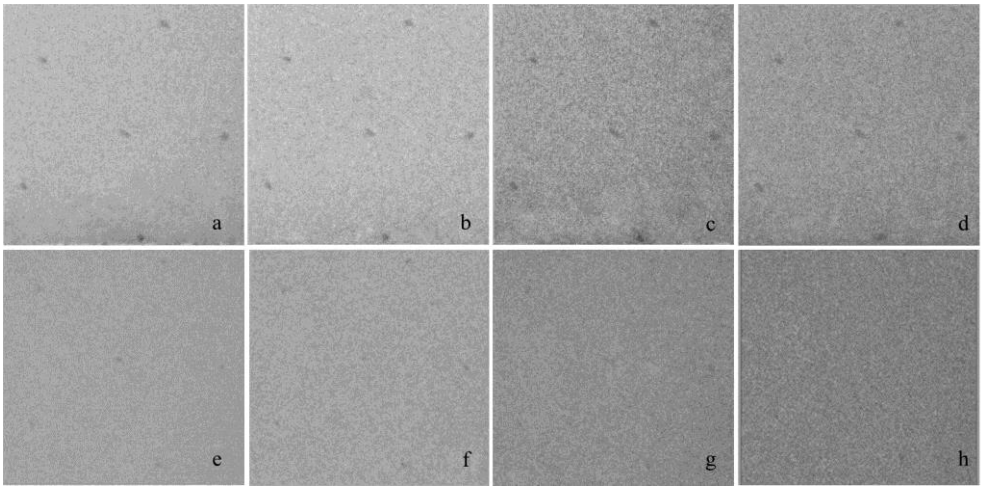

324

325 **Fig. 6.** Sections of the DE images of the accreditation phantom showing the specks
326 groups (7) and (8) at the top and bottom row respectively, for all MGD values.

327

328 The effect of post-process pixel binning on the DE images of ACR phantom is shown
329 in Fig. 7. All specks of speck group (8) are more clearly visible on the binning image
330 with a 4×4 kernel, due to the decreased noise level.

331

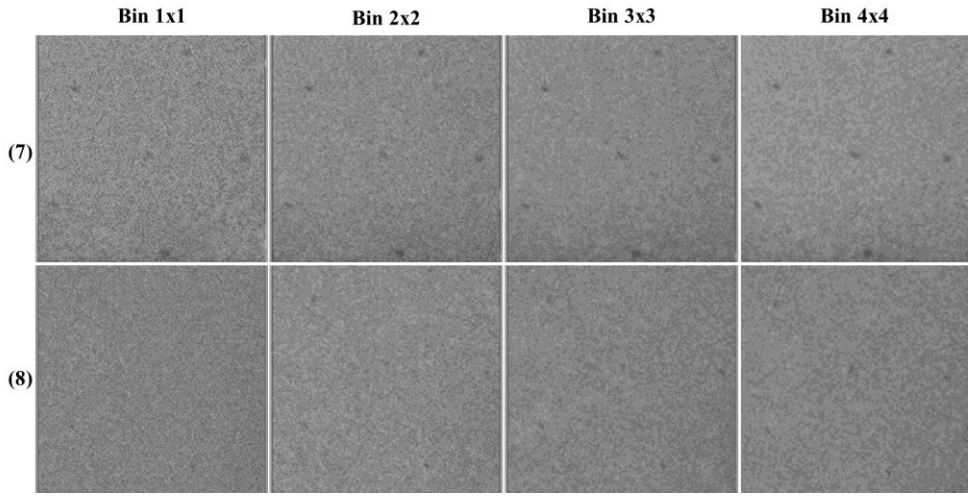

Fig. 7. Sections of the post-processed DE images of the accreditation phantom showing the specks groups (7) and (8) for MGD value of 1.62 mGy.

4. Discussion and Conclusions

The main advantage of DE imaging is the ability to depict calcifications in a largely uniform background, where tissue structures (anatomical noise) have been suppressed [10] and [18]. In single energy techniques, the visible calcification thickness varies across the image [18] and [45]. When complex tissue structures are present, the visible calcification thickness increases [46]. On the other hand, when dual energy techniques are applied the visible calcification thickness is not changing across the image due to the suppression of tissue structures. Under the current implementations of DEDM, the minimum detectable μC size ranges from 300 to 355 μm [10],[19] and [45]. After noise reduction techniques, the minimum μC size was decreased to 250 μm [19].

The CNR values depend on various factors such as irradiation conditions, dose to the subject and most importantly the size of the object [47]. For specific contrast and noise, when the shape of the object is the same but the size decreases, larger objects are more effectively visible compared to the smaller ones [47]. In the present DE study, the CNR in the subtracted images was calculated for various ESDs and breast phantoms, in order to determine the minimum detectable calcification.

In the case of the custom-made calcification phantoms, the thicknesses of the circular objects reproduce the absorption of μCs and not their sizes. The calcification CNR calculated for this phantom is expected to be higher than that of a spherical small size object. In the latter case, the mean pixel value (MPV) ranges from a peak,

357 corresponding to the attenuation from the maximum thickness of the sphere, to a pixel
358 value close to that of the background. Thus, the MPV will be lower than that of a
359 circular cylindrical object (custom-made calcification phantom) where the radiation
360 attenuates along its longitudinal axis. Each pixel value of this circular cylindrical
361 object will be almost equal to the peak pixel value of the spherical object.
362 Additionally, the pixel pitch will have a significant impact in degrading the CNR
363 value when it is comparable to that of a small size object. In our study, this effect is
364 reduced by the use of a CMOS detector with small pixel pitch (22.5 μm). For
365 example, if a spherical μC is irradiated with a diameter from 150 to 500 μm, the μC
366 diameter length will span across approximately from 7 to 22 pixels. Under these
367 conditions, the pixel values of the central area will be close to maximum.
368 In both breast phantoms, an inversion can be observed between the CNR_{DE} values of
369 DE images acquired with 3.06 and 2.11 mGy (Table 4). In addition to the total
370 entrance dose, the dose allocation between the low- and high-energy exposures affects
371 the calculation of CNR in the DE subtracted images. Based on a previous simulation
372 study, it was found that the optimal low-energy dose ratio, LDR (defined as low-
373 energy dose over total dose) ranged from 0.2 to 0.65 [29]. In the case of 3.06 mGy,
374 the LDR was 0.75 which was above the optimal range. On the contrary, for 2.11 mGy,
375 the LDR was 0.54 that falls within this range [29].
376 In the case of the lowest examined MGD (1.62 mGy), the DE images of the
377 inhomogeneous breast phantom were further processed and the CNR_{DE} was
378 recalculated. Hardware pixel binning (on-chip) is designed to increase the sensitivity
379 of an image sensor by combining multiple pixels into one larger pixel in the expense
380 of spatial resolution loss [48]. On the other hand, software pixel binning (off-chip)
381 combines multiple pixel values after the signal read out. The result of the off-chip
382 pixel binning can be considered as a filtered version of the input image where the
383 details are smoothed [48]. Between the two methods, there is a slight difference in the
384 image quality, however the spatial resolution of the off-chip method is better [49].
385 Comparing the different examined kernels, post-process pixel binning with a 4×4
386 kernel resulted in higher CNR_{DE} values, approximately 3 times that of the original DE
387 image (Table 5). Furthermore, calcification of 31 μm was clearly shown due to the
388 decrease of image noise (Fig. 5). Similar to the findings for the inhomogeneous

calcification phantom, image noise was decreased in the 4×4 binned image of the ACR phantom and as a result all the specks of group (8) were clearly visible (Fig. 7).

The speck groups of the ACR phantom, corresponding to hydroxyapatite attenuation of 138.90, 104.14 and 69.40 μm were not visible due to the fact that the phantom specks are composed of aluminum oxide (Al_2O_3, density 3.97 g/cm^3) instead of calcium compound, such as hydroxyapatite. The low-/high-energy linear attenuation coefficient ratio of Al_2O_3 is 4.287, while in a Ca compound (i.e. hydroxyapatite) this ratio equals to 6.484. This value for Ca differs more than 50% from the value corresponding to aluminum oxide. Thus, when an Al compound is used instead of Ca, the unknown variables' coefficients of the linear equations system obtain from the Beer-Lambert low [10] and [50] derived from Al compound, adipose and glandular tissue are less different than those derived from Ca compound, adipose and glandular tissue, resulting in limited speck visibility. Phantoms with Ca compound specks would be more appropriate for DE studies; however they were not available in our laboratory.

The improvement in visualization of calcifications, in the current method, is attributed to the use of higher kV X-rays from a modified radiographic unit with heavy filtering leading to larger spectral separation, while preserving MGD within acceptable levels [51]. MGD can be reduced when the filter thickness increases and/or low- and high-energy tube voltages decrease. This cannot be applied using commercially available mammographic or radiographic units, since an increase in filter thickness demands higher X-ray fluence. Furthermore, as indicated by initial simulation studies [29], the optimum kV combination for low- and high-energy (35/70 kV) cannot be applied in commercial units, since they operate either in the range of 20-49 kV (mammography) or in the 40-150 kV range (radiography). On the other hand, the use of two different units cannot be easily accomplished not only due to the misregistration of the focal spots between the two acquired images, but the complete imaging geometry. A modified unit with tungsten anode and X-ray tube voltage ranging from 20 to 70 kV would be a preferable solution to these issues. Additionally, a focal spot size of 0.6 mm, used in this work, reduces the spatial resolution compared to the typical mammographic focal spot sizes (0.1 mm, small and 0.3 mm, large). However, the use of smaller focal spot sizes will require extended exposure times leading to excessive heat load. Thus, an X-ray tube with focal spot size smaller than 0.3 mm and advanced

loading capability is preferable. Another solution to improve resolution, while keeping the 0.6 mm focal spot size, would be increasing the SDD, which subsequently decreases the penumbra. In this case, photon flux will be reduced. A compromise between kV range, exposure time, focal spot size and SDD, is an open issue for the manufacturing of a dedicated X-ray system. Furthermore, calcification visibility could be improved with the use of antiscatter grid, in the expense of increased dose to the patient [9]. A radiographic system considering all the above (kV range, exposure time, focal spot size and SDD) would improve calcification visibility in DE images. Additionally, using such a radiographic system, the masses will also be depicted in the LE images, since mean energies similar to that of the conventional mammography can be used.

In the future, the proposed DE method will be further assessed by phantoms of different glandularities. Also, a special custom-made phantom with various μC sizes will be constructed and it is expected that the CNR values will be degraded compared to that of the current custom-made phantom. Moreover, commercially available medical detector and CMOS APS X-ray detector with larger dimensions and advanced characteristics [25],[26],[27],[52] and [53] will be used.

Acknowledgements

This work was supported by Grant E.040 from the Research Committee of the University of Patras (Programme K. Karatheodori).

References

[1] World Health Organization. World Cancer Report 2014; 2014.

[2] World Health Organization. World Health Statistics 2008; 2008.

[3] J. G. Elmore, K. Armstrong, C. D. Lehman, and S. W. Fletcher, JAMA, 293 (2005), p. 1245.

[4] X. D. Cheng, X. Cai, X. Chen, L. Hu, and X. Lou, Pattern Recogn., 36 (2003), p. 2967.

[5] R. Baker, K. D. Rogers, N. Shepherd, and N. Stone, BJC, 103 (2010), p. 1034.

[6] R. Cox and M. P. Morgan, Bone, 53 (2013), p. 437.

[7] S. Hofvind, B. Iversen, L. Eriksen, B. Styr, K. Kjellevold, and K. Kurz, Acta Radiol., 52 (2011), p. 481.

[8] E. A. Sickles, Recent Results Cancer Res., 119 (1990), p. 88.

[9] A. Taibi and S. Vecchio., Breast Imaging, in *Comprehensive Biomedical Physics, Vol. 2,* in A. Brahme, Editor in Chief (Amsterdam: Elsevier, 2014), p. 121-154.

[10] M. R. Lemacks, S. C. Kappadath, C. C. Shaw, X. Liu, and G. J. Whitman, Med. Phys., 29 (2002), p. 1739.

[11] D. S. Brettle and A. R. Cowen, Phys. Med. Biol., 39 (1994), p. 1984.

[12] M. S. Soo, E. L. Rosen, J. Q. Xia, S. Ghate, and J. A. Baker, Am. J. Roentgenol., 184 (2005), p. 887.

[13] P. C. Johns and M. J. Yaffe, Med. Phys. 12 (1985), p. 289.

[14] M. Marziani, A. Taibi, A. Tuffanelli, and M. Gambaccini, Phys. Med. Biol., 47 (2002), p. 305.

[15] A. Taibi, S. Fabbri, P. Baldelli, C. di Maggio, G. Gennaro, M. Marziani, A. Tuffanelli, and M. Gambaccini, Phys. Med. Biol., 48 (2003), p. 1945.

[16] M. E. Brandan and V. R. Ramirez, Phys. Med. Biol., 51 (2006), p. 2307.

[17] S. C. Kappadath and C. C. Shaw, Phys. Med. Biol., 49 (2004), p. 2563.

[18] S. C. Kappadath and C. C. Shaw, Med. Phys., 32 (2005), p. 3395.

[19] S. C. Kappadath and C. C. Shaw, Phys. Med. Biol., 53 (2008), p. 5421.

[20] P. C. Johns, D. J. Drost, M. J. Yaffe, and A. Fenster, Med. Phys., 12 (1985), p. 297.

[21] J. M. Boone and G. S. Shaber, Med. Phys., 17 (1990), p. 665.

[22] T. Asaga, C. Masuzawa, A. Yoshida, and H. Mattsuura, J. Digit. Imaging, 8 (1995), p. 70.

[23] P. Baldelli, A. Bravin, C. Di Maggio, G. Gennaro, M. Gambaccini, A. Sarnelli, and A. Taibi, Nucl. Instrum. Meth. Phys. Res. A, 580 (2007), p. 1115.

[24] C. Dromain, F. Thibault, F. Diekmann, E. Fallenberg, R. Jong, M. Koomen, R. E. Hendrick, A. Tarvidon, and A. Toledano, Breast Cancer Res., 14 (2012), R94.

[25] A. C. Konstantinidis, M. B. Szafraniec, R. D. Speller, and A. Olivo, Nucl. Instr. Meth. Phys. Res. A, 689 (2012), p. 12.

[26] M. Szafraniec, A. Konstantinidis, G. Tromba, D. Dreossi, S. Vecchio, L. Rigon, N. Sodini, S. Naday, S. Gunn, A. McArthur, and A. Olivo, Phys. Medica, 31 (2014), p. 192.

[27] C. Zhao, J. Kanicki, A. C. Konstantinidis, and T. Patel, Med. Phys., 42 (2015), p. 6294.

[28] C. M. Michail, N. E. Kalyvas, I. G. Valais, G. P. Fountos, N. Dimitropoulos, G. Koulouras, D. Kandris, M. Samarakou, and I. Kandarakis, BioMed. Res. Int., doi:10.1155/2014/634856 (2014).

[29] V. Koukou, N. Martini, C. Michail, P. Sotiropoulou, C. Fountzoula, N. Kalyvas, I. Kandarakis, G. Nikiforidis, and G. Fountos, Comput. Math. Methods Med., (2015) 574238.

[30] V. Koukou, G. Fountos, N. Martini, P. Sotiropoulou, C. Michail, N. Kalyvas, I. Valais, A. Bakas, E. Kounadi, I. Kandarakis, and G. Nikiforidis, "Optimization of breast cancer

492 detection in Dual Energy X-ray Mammography using a CMOS imaging detector," J.
493 Phys. Conf. Ser., 574 (2015), 012076.
494 [31] N. Martini, V. Koukou, C. Michail, P. Sotiropoulou, N. Kalyvas, I. Kandarakis, G.
495 Nikiforidis, and G. Fountos, Journal of Spectroscopy, (2015) 563763.
496 [32] P. Sotiropoulou, G. Fountos, N. Martini, V. Koukou, C. Michail, I. Kandarakis, and G.
497 Nikiforidis, Phys. Medica, 31 (2015), p. 307.
498 [33] Del Medical Systems Group, Roselle, IL [Online]. Available from:
499 http://www.delmedical.com.
500 [34] C. M. Michail, V. A. Spyropoulou, G. P. Fountos, N. I. Kalyvas, I. G. Valais, I. S.
501 Kandarakis, and G. S. Panayiotakis G, IEEE Trans. Nucl. Sci., 58 (2011), p. 314.
502 [35] Seferis, C. Michail, I. Valais, G. Fountos, N. Kalyvas, F. Stromatia, G. Oikonomou, I.
503 Kandarakis, and G. Panayiotakis, Nucl. Instrum. Meth. Phys. Res. A, 729 (2013), p. 307.
504 [36] C. M. Michail, G. P. Fountos, P. F. Liaparinos, N. Kalyvas, I. Valais, I. Kandarakis, and
505 G. S. Panayiotakis, Med. Phys., 37 (2010), p. 3694.
506 [37] ACR 1999 Mammography, Quality Control Manual (Reston, VA: American College of
507 Radiology).
508 [38] M. Boone, Radiology, 213 (1999), p. 23.
509 [39] L. Ducote, T. Xu, and S. Molloi, Phys. Med. Biol., 52 (2007), p. 183.
510 [40] X. Mou, X. Chen, L. Sun, H. Yu, Z. Ji, and L. Zhang, Phys. Med. Biol., 53 (2008), p.
511 6321.
512 [41] M. Freed, J. A. de Zwart, J. T. Loud, R. H. El Khouli, K. J. Myers, M. H. Greene, J. H.
513 Duyn, and A. Badano, Med. Phys., 38 (2011), p. 743.
514 [42] M. Freed, A. Badal, R. Jennings, H. de las Heras, K. Myers, and A. Badano, Phys. Med.
515 Biol., 56 (2011), p. 3513.
516 [43] J. K. Gong, J. S. Arnold, and S. H. Cohn, Anat. Rec., 149 (1964), p. 319.
517 [44] http://www.imagingequipment.co.uk/product/1357-81/Mammographic-Accreditation-
518 Phantom-Gammex-156 (last accessed 15 December 2016).
519 [45] C. J. Lai, C. C. Shaw, G. J. Whitman, D. A. Johnston, W. T. Yang, V. Selinko, E.
520 Arribas, B. Dogan, and S. C. Kappadath, Med. Phys., 32 (2005), p. 183.
521 [46] K. M. Kelly, J. Dean, W. S. Comulada, and S. J. Lee, Eur. Radiol., 20 (2010), p. 734.
522 [47] A. Konstantinidis, Physical Parameters of Image Quality, in *Comprehensive Biomedical*
523 *Physics, Vol. 2,* in A. Brahme, Editor in Chief (Amsterdam: Elsevier, 2014), p. 49-63.
524 [48] Y. Yoo, J. Im, and J. Paik, Sensors, 15 (2015), p. 14917.
525 [49] J. Farrell, M. Okincha, M. Parmar, and B. Wandell, "Using visible SNR (vSNR) to
526 compare the image quality of pixel binning and digital resizing," Proc of SPIE-IS&T
527 Electronic Imaging, 7537 (2010), 75370C.
528 [50] G. Fountos, S. Yasumura, and D. Glaros, Med. Phys., 24 (1997), p. 1303.

[51] Code of Federal Regulations, Title 21, Chapter I, Subchapter I, Part 900, Subpart B-Quality Standards and Certification, §900.12, revised April 1, 2015.

[52] A. C. Konstantinidis, M. B. Szafraniec, L. Rigon, G. Tromba, D. Dreossi, N. Sodini, P. F. Liaparinos, S. Naday, S. Gunn, A. McArthur, R. D. Speller, and A. Olivo, IEEE Trans. Nucl. Sci., 60 (2013), p. 3969.

[53] C. Michail, I. Valais, N. Martini, V. Koukou, N. Kalyvas, A. Bakas, I. Kandarakis, G. Fountos, Radiat. Meas., 94 (2016), p. 8.